Impedance spectroscopic analysis of the electrochemical methanol oxidation kinetics

U. Krewer [a], M. Christov [a,b], T. Vidakovic' [a,c], K. Sundmacher [a,d,*]

[a] *Max Planck Institute (MPI) for Dynamics of Complex Technical Systems, Sandtorstraße 1, 39106 Magdeburg, Germany*
[b] *University of Chemical Technology and Metallurgy, Department of Physical Chemistry, 1756 Sofia, Bulgaria*
[c] *Faculty of Technology and Metallurgy, Karnegijeva 4, 11120 Belgrade, Serbia and Montenegro*
[d] *Otto von Guericke University Magdeburg, Process Systems Engineering, Universitätsplatz 2, 39106 Magdeburg, Germany*

Abstract

This paper presents a dynamic analysis of the methanol oxidation kinetics on a direct methanol fuel cell anode in a cyclone flow cell. Four kinetic descriptions for methanol oxidation are discussed. They differ in the adsorption/desorption mechanisms, as well as in the potential dependence of a reaction step. Since all kinetic descriptions quantitatively describe the experimental steady state behaviour, dynamic measurements, here electrochemical impedance spectroscopy, is used for model discrimination. The presented impedance spec tra are modelled by using the frequency domain transformed balance equations of the four kinetic descriptions. Analysis of the depen dence of the modelled impedance spectra on parameter variation shows a narrow range in which pseudo inductive behaviour is produced: at least two consecutive steps with similarly fast reactions have to be involved. Besides reaction rate constants, storage param eters and anode potential also show a strong influence on the impedance spectra. The parameters of all four kinetic descriptions have been globally optimised. A comparison of the resulting impedance spectra leads to the identification of the best quantitative description of the electrochemical methanol oxidation kinetics.

Keywords: Direct methanol fuel cell; EIS; Transfer function; Model discrimination

1. Introduction

The direct methanol fuel cell (DMFC) has important advantages to the hydrogen fuel cell, the fuel is liquid, hence it can be more easily stored and handled, and it has a higher energy density. None-the-less, the oxidation of methanol at the low operating temperatures of the DMFC ($\leqslant$400 K) is significantly slower than hydrogen oxidation. The decomposition of methanol, in gross

$$CH_3OH + H_2O \rightarrow 6H^+ + 6e^- + CO_2 \quad (1)$$

can only proceed via various reaction steps. At least one of these steps involves a strongly adsorbed intermediate which slows down the oxidation rate. A vast amount of research on methanol oxidation can be found in the literature [1 13]. Most of the research nowadays is conducted on binary Pt/Ru catalysts [6 9], since they seem to be the most active catalysts for methanol oxidation. The addition of small amounts of other metals, see [14 16], showed no significant improvement of the catalyst activity. It is accepted that the enhancement of the reaction rate for methanol oxidation on PtRu catalyst compared to pure Pt catalyst is due to a bifunctional mechanism [17] where Pt is responsible for methanol adsorption and dehydrogenation, and Ru for OH adsorption which commences at lower overpotentials than on platinum itself [18]. As a further reason, an electronic effect between Pt and Ru decreases the strength of

* Corresponding author. Tel.: +49 391 6110 350; fax: +49 391 6110 353.
E mail addresses: krewer@mpi magdeburg.mpg.de (U. Krewer), chr@uctm.edu (M. Christov), vidakovi@mpi magdeburg.mpg.de (T. Vidakovic'), sundmacher@mpi magdeburg.mpg.de (K. Sundmacher).

0022 0728/$ see front matter
doi:10.1016/j.jelechem.2006.01.027

Nomenclature

A	system matrix
A_s	geometric electrode area, 2.14×10^{-4} m^2
B	input vector
c_{CH_3OH}	methanol concentration in anode catalyst layer, mol/m^3
c_{Pt}, (c_{Ru})	surface concentration of Pt, (of Ru), mol/m^2
C	output vector
C_{dl}	anode double layer capacitance, C/m^2
D	direct transmission parameter
E	anode potential, V
f	frequency, Hz
g_{CO}, (g_{OH})	inhomogeneity/interaction factor for Frumkin/Temkin adsorption on Pt, (on Ru)
F	Faraday constant, 96,485 C/mol
G	transfer function
j	imaginary unit
j_{cell}	cell current density, A/m^2
$k_{i,0}$	reaction rate constant for reaction i
k_i^{eff}	effective reaction rate function for reaction i
R	universal gas constant, 8.314 J/mol/K
s	Laplace variable
t	time, s
T	cell temperature, K
u, (U)	input variable (in Laplace domain)
x, (X)	state variable (in Laplace domain)
y, (Y)	output variable (in Laplace domain)
Z	electrochemical impedance, Ω
α_{ai}	charge transfer coefficient for anodic reaction i
β_{CO}, (β_{OH})	symmetry parameter for Frumkin/Temkin adsorption on Pt, (Ru)
θ_{CO}	surface coverage of Pt with CO_{ads}
θ_{OH}	surface coverage of Ru with OH_{ads}

subscripts

A	anode
ACO	anode CO_{ads} surface coverage on Pt
AE	anode potential
AOH	anode OH_{ads} surface coverage on Ru
i	counter

superscripts

$\ominus$	reference state

the bond between an adsorbed intermediate and the Pt surface. This increases the reaction rate on PtRu catalyst compared to pure Pt even for the same surface coverage of CO and OH [19].

Knowledge of the reaction mechanism is relevant for understanding and optimising the DMFC behaviour. In [20], the authors analysed the cell voltage response of the DMFC to cell current steps, finding a very intense dynamic behaviour with overshoots of ~30% (Fig. 1, concatenated symbols). Simulations with a simple one-step reaction mechanism (Fig. 1, dotted line) or a consecutive two-step reaction mechanism (Fig. 1, solid line) cannot quantitatively reproduce the behaviour, but they show that the anodic methanol reaction mechanism has a strong influence on the dynamic behaviour. Furthermore, understanding the mechanism may help generating better catalysts as well as developing a special control strategy to improve the power output, e.g., by periodically removing adsorbed species.

Most investigations on the reaction mechanism of methanol oxidation are conducted on non-technical electrodes, e.g., on single crystals or smooth surfaces [2 5,10 13]. They focus on the detection of adsorbed species or products. Using different analysis techniques (CV, FTIR, FTIR-DRS, DEMS, etc.), more than 10 adsorbed methanol derivates were detected or postulated: $(CO)_{ads}$, $(COH)_{ads}$, $(CHO)_{ads}$, $(COOH)_{ads}$, $(OCH)_{ads}$, $(OCH_2)_{ads}$, $(OCH)_{ads}$, $(CHOH)_{ads}$, $(CH_2OH)_{ads}$, and $(CH_3OH)_{ads}$. Due to the deviation of the experimental conditions to real fuel cell conditions (electrode structure, temperature, additional

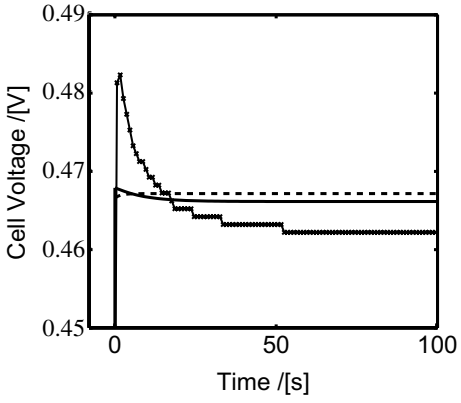

Fig. 1. Response of the DMFC to a current step down experiment (concatenated symbols) vs. DMFC model with a single reaction step (dashed line) and vs. DMFC model with a consecutive reaction mecha nism (solid line), details see [20].

chemicals, no diffusion layer, etc.), they are not all equally important for the reaction inside the DMFC. Summarising the main experimental findings in the literature, the reaction pathways given in Fig. 2 can be formulated.

The aim of this work is to use electrochemical impedance spectroscopy as a dynamic method for model discrimination. A lumped reaction mechanism based on the reaction scheme above is discussed. The mechanism should be able to qualitatively and quantitatively describe the steady-state and dynamic behaviour of the methanol oxidation on Pt/Ru fuel cell catalysts for DMFCs. The reaction mechanism and four different kinetic formulations are

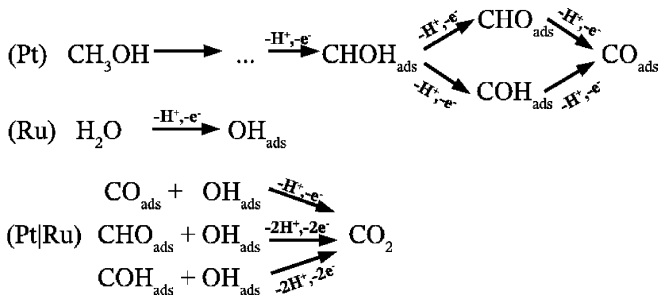

Fig. 2. Main reaction pathways of methanol oxidation.

based on assumptions made in [6]. All models can quantitatively reproduce the steady-state experiments, but not the dynamic behaviour. Impedance spectra are modelled by using frequency domain transformed transfer functions generated from balance equations. In contrast to equivalent circuit models, these models do not contain empirical elements. An in-depth investigation of the parameter influence on the impedance spectra is presented, highlighting the complex influence of the parameters on the EIS. Recorded electrochemical impedance spectra are used for model discrimination, and a quantitative reaction kinetic model is identified.

2. Experimental

2.1. Production of MEAs

The membrane electrode assembly (MEA) is prepared from NAFION™ N-105 membrane foil, onto which the catalyst layers are applied using an airbrush technique developed by ZSW Ulm (Germany) [21]. The anode catalyst layer features a catalyst loading of 5 mg/cm^2 (unsupported) platinum ruthenium black (Alfa Aesar Johnson Matthey HiSPEC™ 6000) and a NAFION™ content of 15 mass% relative to the metal loading (i.e. 0.75 mg/cm^2). As diffusion layer PTFE-coated TORAY carbon paper (TGP-H-060) is used, with a PTFE loading between 20 and 25 mass% with respect to the uncoated material. The MEA was hot pressed at 403 K at a pressure of 10 MPa during 3 min onto the TORAY carbon paper. The total geometric area of the MEA covered by the catalyst layer was 12.56 cm^2, but only 2.14 cm^2 were exposed to the anode and cathode compartment.

2.2. Experimental setup

The measurements were conducted in a half cell setup [6] which resembles an idealised anode of a DMFC: it contains a MEA and shows minimal mass transport and cathode influence, as explained in the following. (a) The setup is a cyclone flow cell, see Fig. 3. Like in a fuel cell, a DMFC MEA separates the anode and cathode compartment. So the results can be directly used in complete DMFC models. (b) The flow pattern inside the compartments is similar to the flow inside a cyclone, causing a homogeneous concentration distribution over the MEA. (c) The setup enables measurements at a defined anode potential by using a reference electrode.

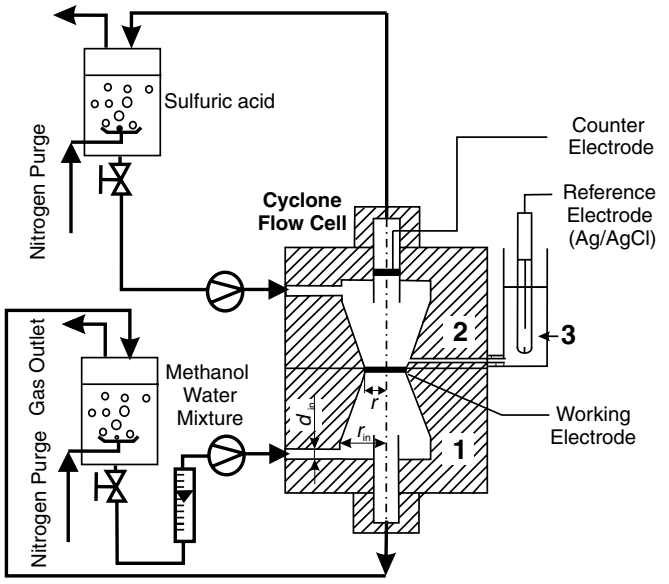

Fig. 3. Schematic representation of the experimental setup: 1 working electrode compartment, 2 counter electrode compartment, 3 reference electrode compartment.

The cyclone flow cell consists of three compartments: working electrode compartment (1), counter electrode compartment (2) and reference electrode compartment (3). The reference electrode was saturated silver/silver chloride (0.196 V vs. SHE). All potentials in this paper were recalculated vs. SHE. The working electrode compartment was supplied with reactants (methanol/water mixture with different methanol concentrations), while the counter electrode (2) and the reference electrode (3) compartments were supplied with 1 M sulphuric acid solution. The reference electrode compartment was connected to the counter electrode compartment by a Luggin capillary. Due to the electric current in the liquid layer between the end of the Luggin capillary and the catalyst layer, the measured working electrode potential was corrected for corresponding Ohmic drop (see below). The electrolyte solutions are prepared from sulphuric acid (Merck, extra pure), methanol (Merck, extra pure) and ultrapure water (Millipore, 18 MΩ cm). Working electrode compartment and counter electrode compartment supply containers were deaerated with nitrogen, and the deaerated solutions were circulated through the cell.

All electrochemical measurements were carried out with a Zahner impedance measurement unit (IM6e). Experiments were performed at a temperature of 333 K. The cell temperature was controlled by use of a Julabo F12 thermostat. For all electrochemical measurements, preconditioning of the membrane electrode assembly (MEA) was done by cyclic voltammetry in the potential range from 0 to 0.7 V at a sweep rate of 20 mV s^{-1}. Five cycles were enough to obtain a reproducible MEA behaviour.

2.3. Impedance measurements

For impedance measurements, the potential was stopped after preconditioning at the desired set point, and the current was recorded over time (30 min in methanol containing solution). Impedance measurements were performed immediately afterwards at the same DC potential, over a frequency range between 2 kHz and 10 mHz. The amplitude of the sinusoidal signal was 5 mV (from base to peak). The measurements were corrected for Ohmic drop by subtracting the Ohmic resistance (impedance at high frequencies) from the real part of the impedance data.

3. Reaction mechanism and four kinetic descriptions

Based on the reaction pathways given above and on the literature findings, the following mechanism for methanol oxidation was formulated in [6]:

$$(\mathrm{Pt})\ \mathrm{CH_3OH} \xrightarrow{k_1} \mathrm{CH_3OH_{ads}} \rightarrow \ldots \xrightarrow{-3\mathrm{H}^+-3\mathrm{e}} \mathrm{CO_{ads}} + \mathrm{H}^+ + \mathrm{e}^- \tag{2}$$

$$(\mathrm{Ru})\ \mathrm{H_2O} \underset{k_{-2}}{\overset{k_2}{\rightleftharpoons}} \mathrm{OH_{ads}} + \mathrm{H}^+ + \mathrm{e}^- \tag{3}$$

$$(\mathrm{Pt/Ru})\ \mathrm{CO_{ads}} + \mathrm{OH_{ads}} \xrightarrow{k_3} \mathrm{CO_2} + \mathrm{H}^+ + \mathrm{e}^- \tag{4}$$

Vidakovic' et al. [6] could show that mass transport resistance from the anode compartment to the catalyst layer can be neglected when using the presented experimental setup. The first modelling relevant mechanistic step is therefore the partial oxidation of methanol, shown in Eq. (2): methanol physisorbs at Pt and is subsequently decomposed to CO_{ads} by H-atom extraction. This process is supposed to occur only on the Pt adsorption sites. In a parallel reaction step (Eq. (3)), OH species are formed by water dissociative adsorption on the Ru adsorption sites. The third reaction step (Eq. (4)) represents the surface reaction between OH_{ads} and CO_{ads}, leading to CO_2 evolution. The surface then is set free for new methanol and water adsorption.

To analyse the methanol oxidation kinetics, non-linear mathematical models based on the above given reaction mechanism were developed accounting for the following phenomena:

- Irreversible electrochemical partial oxidation of methanol to the adsorbed intermediate CO_{ads}.
- Reversible electrochemical partial oxidation of water to the adsorbed intermediate OH_{ads}.
- Irreversible electrochemical or chemical reaction of adsorbed CO_{ads} and OH_{ads} to CO_2.

The following model assumptions are made:

- The methanol concentration in the anode catalyst layer is identical to the methanol feed concentration (minimised mass transport influences in the cyclone flow cell [6]).
- In the given temperature range, methanol adsorption occurs only on Pt.
- For the electrochemical partial oxidation of methanol (Eq. (2)), the first step (potential independent methanol physisorption) is considered to be the rate-determining step.
- In the given temperature range, water adsorption occurs only on Ru.
- Water concentration is constant since it is an excess component.
- A pure liquid phase mixture is assumed, i.e. gas-phase formation by release of carbon dioxide bubbles is not taken into account. Problems with bubble formation only get visible when working and modelling in or near the limiting current regime of the polarisation curve, which is not done here.
- Ohmic drop is zero, since experiments have already been corrected.

Based on the assumptions given above, balance equations for the surface coverage of the adsorbed intermediates CO_{ads} (Eq. (5)) and OH_{ads} (Eq. (6)), as well as for the anodic potential E (Eq. (7)) are formulated:

$$c_{\mathrm{Pt}} \cdot \frac{\mathrm{d}\theta_{\mathrm{CO}}}{\mathrm{d}t} = k_1^{\mathrm{eff}}(\theta_{\mathrm{CO}}) \cdot c_{\mathrm{CH_3OH}} \cdot (1-\theta_{\mathrm{CO}}) - k_3^{\mathrm{eff}}(E,\theta_{\mathrm{CO}}) \cdot \theta_{\mathrm{CO}} \cdot \theta_{\mathrm{OH}} \tag{5}$$

$$c_{\mathrm{Ru}} \cdot \frac{\mathrm{d}\theta_{\mathrm{OH}}}{\mathrm{d}t} = k_2^{\mathrm{eff}}(E,\theta_{\mathrm{OH}}) \cdot (1-\theta_{\mathrm{OH}}) - k_{-2}^{\mathrm{eff}}(E,\theta_{\mathrm{OH}}) \cdot \theta_{\mathrm{OH}} - k_3^{\mathrm{eff}}(E,\theta_{\mathrm{CO}}) \cdot \theta_{\mathrm{CO}} \cdot \theta_{\mathrm{OH}} \tag{6}$$

$$C_{\mathrm{dl}} \cdot \frac{\mathrm{d}E}{\mathrm{d}t} = j_{\mathrm{cell}} - F[4 \cdot k_1^{\mathrm{eff}}(\theta_{\mathrm{CO}}) \cdot c_{\mathrm{CH_3OH}} \cdot (1-\theta_{\mathrm{CO}}) + k_2^{\mathrm{eff}}(E,\theta_{\mathrm{OH}}) \cdot (1-\theta_{\mathrm{OH}}) - k_{-2}^{\mathrm{eff}}(E,\theta_{\mathrm{OH}}) \cdot \theta_{\mathrm{OH}} + k_3^{\mathrm{eff}}(E,\theta_{\mathrm{CO}}) \cdot \theta_{\mathrm{CO}} \cdot \theta_{\mathrm{OH}}] \tag{7}$$

θ_{CO} and θ_{OH} are the fractional surface coverages of Pt with CO_{ads}, and Ru with OH_{ads}, respectively, and E is the anode potential. $k_1^{\mathrm{eff}}(\theta_{\mathrm{CO}})$, $k_2^{\mathrm{eff}}(E,\theta_{\mathrm{OH}})$, $k_{-2}^{\mathrm{eff}}(E,\theta_{\mathrm{OH}})$, and $k_3^{\mathrm{eff}}(E,\theta_{\mathrm{CO}})$ are the effective reaction rate functions for reaction $i \in \{1,2,-2,3\}$. These rate functions contain different kinetic descriptions and dependencies on E, θ_{CO} and θ_{OH}. They are defined below in this section. C_{dl}, c_{Pt} and c_{Ru} are the storage capacities for charge, i.e. the double layer capacitance, for CO, i.e. the Pt surface concentration, and for OH_{ads}, i.e. the Ru surface concentration, respectively. Setting the left side of the set of Eqs. (5) (7) to zero results in the steady-state descriptions, in which the storage capacities have no influence. Formally seen, c_{Pt} and c_{Ru} influence the effective reaction rate functions $k_i^{\mathrm{eff}}(E,\theta_{\mathrm{CO}},\theta_{\mathrm{OH}})$, but since these surface concentrations cannot be separated from the reaction kinetic constants at steady-state, they are incorporated in the reaction rate constants (see Section 4.3.3).

In the literature, various dependences of the reaction rates on potential and surface coverage are given [5,7,22 27]. In [6], five kinetic descriptions, assuming different adsorption mechanisms and potential dependences, have

been discussed and compared with regard to their influence on the polarisation curve. Based on these, we here present four kinetic variants, which can be expressed by modifying the reaction rate functions $k_i^{\mathrm{eff}}(E, \theta_{\mathrm{CO}}, \theta_{\mathrm{OH}})$.

The first distinction is done with regard to the potential dependence of reaction step 3 (Eq. (4)): Vidakovic' et al. [6] postulate a potential dependent surface reaction with

$$\mathrm{CO_{ads}} + \mathrm{OH_{ads}} \rightarrow \mathrm{CO_2} + \mathrm{H^+} + \mathrm{e^-} \tag{8}$$

while Kauranen et al. [7] assume a consecutive reaction

$$\mathrm{CO_{ads}} + \mathrm{OH_{ads}} \overset{\text{r.d.s.}}{\rightarrow} \mathrm{COOH_{ads}} \rightarrow \mathrm{CO_2} + \mathrm{H^+} + \mathrm{e^-} \tag{9}$$

where the first reaction, a chemical reaction, is the rate determining step. Hence, reaction step 3 (Eq. (4)) would be potential independent. We will refer to the potential dependent description as VCS (author initials of [6]), and to the potential independent description as Kauranen.

In addition to the potential dependence, we introduce a second distinction with regard to the adsorption/desorption mechanism, which affects all three reaction rate functions. The most frequently used adsorption description, based on mechanistic considerations, is Langmuir adsorption [5,23 27]. Kauranen et al. [7] assume Frumkin/Temkin type adsorption for methanol on the Pt adsorption sites, but at the same time use Langmuir for the adsorption of $\mathrm{OH_{ads}}$. Only in [22], Frumkin/Temkin type adsorption is assumed for all species. The assumption of Langmuir adsorption for $\mathrm{OH_{ads}}$ should yield a well-expressed peak in cyclic voltammograms in the absence of methanol, which was not observed [6]. Hence, in case of introducing a Frumkin/Temkin type adsorption for $\mathrm{CO_{ads}}$, also Frumkin/Temkin type adsorption for $\mathrm{OH_{ads}}$ should be adopted. So, the second type of distinction in this manuscript is drawn with regard to the adsorption/desorption mechanism, which is either a Langmuir-type adsorption or a Frumkin/Temkin type adsorption. The type then holds for all reaction steps.

Combining these two types of distinction (potential dependence of third reaction step, adsorption/desorption mechanisms) yields four different kinetic variants: VCS Langmuir, VCS Frumkin/Temkin, Kauranen Langmuir and Kauranen Frumkin/Temkin. Mathematically, the differences between the kinetic descriptions can be summarised in the reaction rate functions $k_1^{\mathrm{eff}}(\theta_{\mathrm{CO}}), k_2^{\mathrm{eff}}(E, \theta_{\mathrm{OH}})$, $k_{-2}^{\mathrm{eff}}(E, \theta_{\mathrm{OH}})$, and $k_3^{\mathrm{eff}}(E, \theta_{\mathrm{CO}})$ for the reactions 1 to 3:

$$k_1^{\mathrm{eff}}(\theta_{\mathrm{CO}}) = k_{1,0} \cdot \exp[-\beta_{\mathrm{CO}} g_{\mathrm{CO}}(\theta_{\mathrm{CO}} - 0.5)] \tag{10}$$

$$k_2^{\mathrm{eff}}(E, \theta_{\mathrm{OH}}) = k_{2,0} \cdot \exp\left[\frac{\alpha_{a2} F}{RT} E\right] \cdot \exp\left[-\beta_{\mathrm{OH}} g_{\mathrm{OH}}(\theta_{\mathrm{OH}} - 0.5)\right] \tag{11}$$

$$k_{-2}^{\mathrm{eff}}(E, \theta_{\mathrm{OH}}) = k_{-2,0} \cdot \exp\left[-\frac{(1-\alpha_{a2}) F}{RT} E\right] \cdot \exp\left[(1-\beta_{\mathrm{OH}}) g_{\mathrm{OH}}(\theta_{\mathrm{OH}} - 0.5)\right] \tag{12}$$

$$k_3^{\mathrm{eff}}(E, \theta_{\mathrm{CO}}) = k_{3,0} \cdot \exp\left[\frac{\alpha_{a3} F}{RT} E\right] \cdot \exp[(1-\beta_{\mathrm{CO}}) g_{\mathrm{CO}}(\theta_{\mathrm{CO}} - 0.5)] \tag{13}$$

Here, $k_{i,0}$ is the reaction rate constant for reaction i with $i \in \{1, 2, -2, 3\}$, and α_{ai} is the charge transfer coefficient for reaction i. The assumption of a Kauranen kinetics yields a potential independent $k_3^{\mathrm{eff}}(\theta_{\mathrm{CO}})$ with α_{a3} 0, whereas for the VCS kinetics $k_3^{\mathrm{eff}}(E, \theta_{\mathrm{CO}})$ is potential dependent with α_{a3} 0.5. The distinction between dependence and independence of the adsorption/desorption energy on surface coverage yields for the first case (Frumkin/Temkin kinetics) an exponential term in all $k_i^{\mathrm{eff}}(E, \theta_{\mathrm{CO}}, \theta_{\mathrm{OH}})$, consisting of the symmetry factor β_i 0.5 (with $i \in \{\mathrm{CO_{ads}}, \mathrm{OH_{ads}}\}$), the inhomogeneity/interaction factor g_i, and the surface coverage. For the case of surface coverage independent adsorption energies, i.e. for the Langmuir kinetics, the inhomogeneity factors are set to zero, i.e. $k_i^{\mathrm{eff}} \neq f(\theta_{\mathrm{CO}}, \theta_{\mathrm{OH}})$.

Steady-state measurements were recorded in [6] at various concentrations between 0.03 and 3 mol/l (at 333 K), as well as at various temperatures between room temperature and 333 K (at 1 mol/l). The measurements have been discussed in detail as well as modelled with the different kinetic models in [6]. All kinetic variants are able to describe satisfactorily the experimental results [6]. Since the steady-state measurements and their concentration and temperature dependence are not sufficient for model discrimination between the kinetic descriptions, electrochemical impedance spectroscopy (EIS) is used.

4. Analysis of the electrochemical impedance spectra

4.1. Experimental results

Electrochemical impedance spectra were recorded at the (Ohmic drop corrected) potentials 0.37, 0.41 and 0.44 V at 333 K, using a 1 M anodic methanol solution. These operating conditions are identical to the conditions at dynamic operation of the DMFC, which allows a good portability of the kinetic results to DMFC models.

The frequency ranges from 2 kHz to 10 mHz. The recorded spectra are presented in Fig. 4 (concatenated symbols). The impedance plots resemble each a depressed semi-

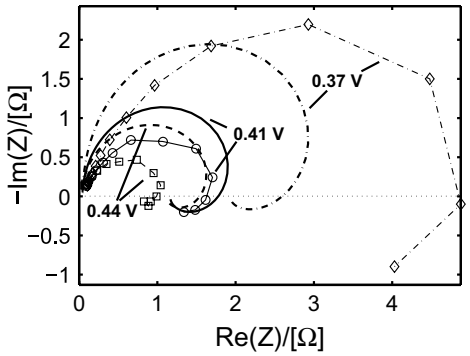

Fig. 4. Simulated EIS (lines) of the VCS Langmuir model with optimised parameters (values see Table 1) vs. experimental EIS (concatenated symbols) at three potentials.

circle and a low frequency pseudo-inductive loop. EIS of depressed semicircle shape characterise surfaces with a high roughness [28]. Increasing the potential, the size of the overall EIS decreases which indicates that the charge transfer resistance for methanol oxidation becomes smaller.

Pseudo-inductive behaviour in the low frequency region has been reported in the literature for methanol oxidation at smooth polycrystalline platinum [29], at carbon-supported Pt-nanoparticles [30] and at Pt/Ru fuel cell anodes [8]. Such pseudo-inductive patterns are known to be a typical feature of systems with adsorbed intermediates or with a transition between a passive and an active state [9].

The observed pseudo-inductive behaviour most probably can be attributed to a particular kinetic phenomenon characterising methanol oxidation. Hence, a good reproduction of the pseudo-inductive behaviour is a precondition for acceptance of a kinetic model.

4.2. Modelling EIS via Laplace transformation

To model the recorded impedance spectra with the kinetic descriptions, the set of equations (Eqs. (5) (7)) is transformed into the frequency domain. In contrast to modelling with equivalent circuit EIS models, such models have a direct physico-chemical relevance, since they do not contain empirical elements. For the SOFC, a similar approach has been done by the group of Gauckler [31], with the difference that the double layer charging influence is added as an equivalent circuit element. The approach applied in this paper is a combination of standard methods used in process dynamics [32] and control engineering [33]. The exact procedure is shown in the following:

After linearisation around the contemplated steady-state, the set of balance equations, Eqs. (5) (7), is cast into the state space form:

$$\frac{\mathrm{d}\mathbf{x}}{\mathrm{d}t} = A\mathbf{x}(t) + Bu(t) \tag{14}$$

$$y(t) = C\mathbf{x}(t) + Du(t) \tag{15}$$

where A, B, C and D are the system matrix, input vector, output vector and direct transmission number (in this case D 0), respectively. $u(t)$ is the perturbed input variable, i.e. in this case the cell current density, $y(t)$ is the observed output variable, i.e. the anode potential response, and $\mathbf{x}(t)$ is the vector of state variables $[\theta_{\mathrm{CO}}(t)\ \theta_{\mathrm{OH}}(t)\ E(t)]^{\mathrm{T}}$.

Laplace transformation ($t \rightarrow s$; $y(t) \rightarrow Y(s)$; $u(t) \rightarrow U(s)$; $\mathbf{x}(t) \rightarrow \mathbf{X}(s)$) of this set of equations yields the transfer function G, which is the ratio of output to input variable:

$$G(s) = Y(s)/U(s) = B(sI - A)^{-1}C + D \tag{16}$$

$Y(s)$ is the Laplace transformed anode potential, $U(s)$ is the Laplace transformed cell current density, and I is the unit matrix. Transfer functions as shown in Eq. (16) are a major tool in linear system analysis for investigating the dynamic behaviour of systems, e.g., of a reactor network.

Instead of calculating the total transfer function $G(s)$ using all equations at once, the system can be decomposed into single modules which are interconnected as shown in the blockdiagram in Fig. 5. The decomposition is done with regard to the different state variables: anodic CO_{ads} surface coverage ($G_{A\mathrm{CO}}$), anodic OH_{ads} surface coverage ($G_{A\mathrm{OH}}$) and anode potential ($G_{A\mathrm{E}}$). The single transfer functions are generated from the balance equation of the respective state variable. This method of decomposition has the advantage that the mathematical description of the single modules can be chosen from within a library. The library contains the various alternative mathematical descriptions for each state variable, and the appropriate description is selected according to the investigated kinetics. This enables easy switching between various reaction mechanisms or between quasi steady-state and dynamic assumptions. In addition, the modules are suitable for direct implementation into DMFC models [20].

In a last step, the transfer function $G(s)$ is transformed into the frequency domain to yield the electrochemical impedance $Z(f)$ by exchanging the Laplace variable s with $\mathrm{j} \cdot 2\pi f$, where j is the imaginary unit and f is the frequency vector [33]. The resulting intensive impedance [$\Omega\ \mathrm{m}^2$] is corrected with the cross sectional electrode area A_s to yield the electrochemical impedance in Ω:

$$Z(f) = \frac{G(s = \mathrm{j} \cdot 2\pi f)}{A_s} \tag{17}$$

4.3. Qualitative parameter studies

The following section shows a qualitative parameter study: The influence of model parameters on the impedance spectra is analysed, as well as the occurrence of pseudo-inductive behaviour.

The parameter influence has been studied for all four kinetic models. Since the qualitative parameter dependence of the impedance spectra is widely similar in all models, we present the VCS Langmuir model results when

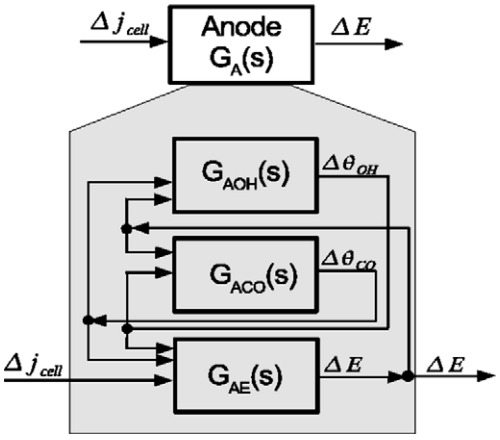

Fig. 5. Representation of the anode catalyst layer as a transfer function block diagram.

investigating parameters that are present in all models, and the VCS Frumkin/Temkin model for the study of the interaction factor influence on the EIS.

4.3.1. Reference spectrum of the VCS Langmuir model

A reference spectrum of the VCS Langmuir kinetics is generated, from which the parameter variations are done. An anode potential of 0.41 V is selected, which is identical to the anode potential of one of the experimental EIS. The following parameters have to be fixed: $k_{i,0}$ ($i \in \{1,2,-2,3\}$), c_{Pt}, c_{Ru} and C_{dl}. The reference reaction rate constants $k_{i,0}^{\ominus}$ are chosen, so that reaction 1 and reaction 3 are similarly fast ($k_1^{\mathrm{eff}} \cdot c_{\mathrm{CH_3OH}} = k_3^{\mathrm{eff}}(E)$), and reactions 2 and -2 are 100 times faster than reaction 1 and reaction 3 ($k_2^{\mathrm{eff}}(E) = k_{-2}^{\mathrm{eff}}(E) = 100 \cdot k_3^{\mathrm{eff}}(E)$). This gives $k_{1,0}^{\ominus} = 1.37 \times 10^{-6}\,\mathrm{m\,s^{-1}}$, $k_{2,0}^{\ominus} = 110 \times 10^{-6}\,\mathrm{mol\,m^{-2}\,s^{-1}}$, $k_{-2,0}^{\ominus} = 171\,\mathrm{mol\,m^{-2}\,s^{-1}}$, $k_{3,0}^{\ominus} = 1.1 \times 10^{-6}\,\mathrm{mol\,m^{-2}\,s^{-1}}$. The double layer capacitance $C_{\mathrm{dl}}^{\ominus}$ ($\approx$1827 F m $^{-2}$) has been experimentally pre-estimated from CV measurements (current vs. sweep rate plot, the difference between anodic and cathodic currents at constant potential (0.3 V) is used to eliminate errors due to a faradaic reaction [34]). Pt and Ru surface concentrations have been roughly estimated ($c_{\mathrm{Pt}}^{\ominus} = c_{\mathrm{Ru}}^{\ominus} = 0.0145\,\mathrm{mol\,m^{-2}}$) by using the BET surface area published in [35].

Fig. 6 shows the simulated spectrum (solid line), as well as the experimental spectrum (concatenated symbols). Although the size of the simulated spectrum is smaller than the experimental one, the simulated spectrum has a shape similar to the experimental one and it also shows pseudo-inductive behaviour. Hence, the given reaction kinetic model with parallel and consecutive reaction steps is able to generate a dynamic behaviour qualitatively similar to the experimentally measured behaviour. The depressed shape of the EIS observed at medium and high frequencies cannot be reproduced by the model, since it results from the non-ideality of the electrode, as discussed in Section 2.

4.3.2. Variation of reaction rate constants

A variation of the reaction rate constants $k_{1,0}$, $k_{2,0}$, $k_{\ 2,0}$ and $k_{3,0}$ shows the influence of a shifting influence of the reaction steps on the EIS. Fig. 7 shows the variation of $k_{1,0}$ from 0.25 times the original value to 10 times the original value. Deviation of $k_{1,0}$ from its original value $k_{1,0}^{\ominus}$, where reaction 1 and reaction 3 are equally influencing the reaction rate, should lead to the preference of either reaction 1 or reaction 3: decreasing $k_{1,0}$ decreases the velocity of step 1, and increases its influence on the overall reaction rate. On the other hand, increasing $k_{1,0}$ decreases its influence, and reaction 3 is the rate determining step (r.d.s). This is clearly visible in the spectra, decreasing $k_{1,0}$ increases the overall impedance, and vice versa. In addition, the pseudo-inductive behaviour depends strongly on $k_{1,0}$, i.e. on the dominance of step 1. Decreasing as well as increasing $k_{1,0}$ leads to vanishing of the pseudo-inductive behaviour. Hence, there is only a small regime in which this phenomenon occurs. According to these findings, a rate determining step (step 1 or step 3) most probably inhibits pseudo-inductive behaviour.

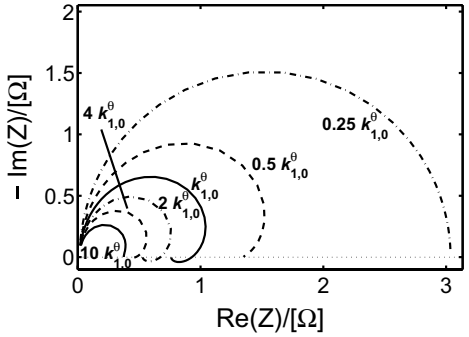

Fig. 7. EIS of the VCS Langmuir model with reaction rate constant $k_{1,0}$ varied from the reference value $k_{1,0}^{\ominus}$.

Variation of $k_{3,0}$ substantiates this hypothesis. The EIS are shown in Fig. 8. Decreasing $k_{3,0}$ leads to a larger overall impedance and to a loss in pseudo-inductive behaviour, since only reaction 3 is determining the overall reaction resistance (reaction 3 is r.d.s.). On the other hand, an increase leads to lower impedance and also to a loss in pseudo-inductive behaviour, i.e. at high $k_{3,0}$, reaction 1 is the rate determining step. Hence, only at roughly equal reaction rates of the two subsequent steps the phenomenon of pseudo-inductance occurs. This finding is in accordance with the result in [6] that there is no single rate determining step in methanol oxidation at medium potentials.

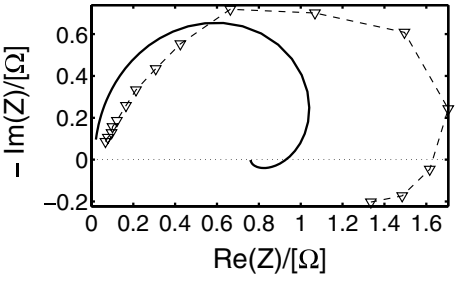

Fig. 6. Reference EIS of the VCS Langmuir model at 0.41 V (line) and experimental EIS (concatenated symbols). Reaction rate constants are selected so that the reaction rates of step 1 and step 3 are equally fast, and reaction 2 is in quasi equilibrium (values see text).

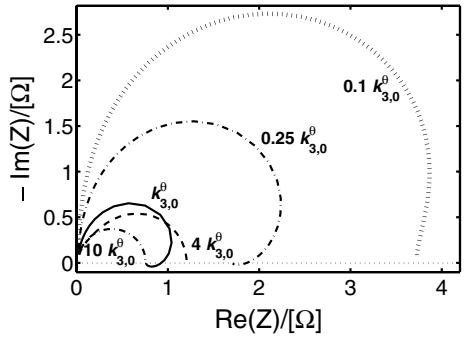

Fig. 8. EIS of the VCS Langmuir model with reaction rate constant $k_{3,0}$ varied from the reference value $k_{3,0}^{\ominus}$.

In contrast to reaction 1 and reaction 3, reaction 2 is supposed to be in quasi equilibrium. The variation of $k_{2,0}$ is shown in Fig. 9. A change in $k_{2,0}$ changes the equilibrium constant, i.e the ratio $k_{2,0}$ to $k_{-2,0}$, producing more or less OH_{ads}, which in turn influences reaction 3. As can be seen, varying $k_{2,0}$ influences the pseudo-inductive behaviour, its size changes, but it is not extinguished. This indicates that the pseudo-inductive behaviour is caused by the subsequent reactions 1 and 3, and it is only indirectly connected to reaction 2 (via OH_{ads}). This is also in accordance with the variation of $k_{1,0}$ and $k_{3,0}$: As long as reaction 1 and reaction 3 are similarly dominating, the model produces pseudo-inductive behaviour.

Finally, Fig. 10 shows the variation of $k_{-2,0}$. The EIS at $n \cdot k_{-2,0}$ (with $n \in \{0.25, 0.1, 4, 10\}$) deviate only slightly from the EIS at $1/n \cdot k_{2,0}$. This substantiates the assumption that a change in $k_{2,0}$ or $k_{-2,0}$ mainly influences the EIS due to the equilibrium constant $k_{2,0}/k_{-2,0}$, but not due to a separate dynamics.

4.3.3. Variation of storage parameters

While the reaction rate constants strongly influence the steady-state and dynamic behaviour, the storage parameters C_{dl}, c_{Pt} and c_{Ru} characterise how fast the mass and charge balances, Eqs. (5) (7), are in a quasi-steady state. i.e. they are not influencing the steady-state, but the dynamic behaviour, hence the EIS.

A variation of the double layer capacitance C_{dl} is shown in Fig. 11. Besides shifting the impedance to different frequencies (only visible in Bode plots), the shape of the EIS changes qualitatively. At high electrochemical capacitance, the shape of the EIS is dominated by the charge balance, since the mass balances are faster in a quasi-steady state than the charge balance. Hence, the influence of the mass balances on the EIS is diminished, and no pseudo-inductance is visible. On the other hand, a minimisation of C_{dl} leads to a pure interaction of the mass balances (5) and (6), since the charge balance is in a quasi-steady state. This is also indicated by the more prevalent pseudo-inductive behaviour. At the reference parameter values therefore, all three balances are influencing the EIS.

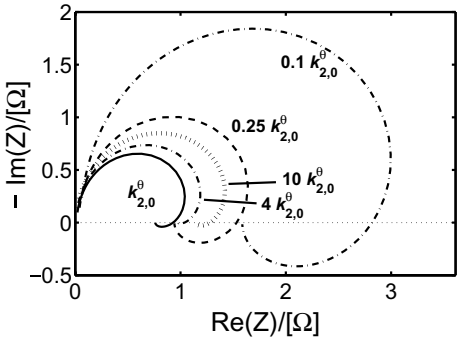

Fig. 9. EIS of the VCS Langmuir model with reaction rate constant $k_{2,0}$ varied from the reference value $k^{\ominus}_{2,0}$.

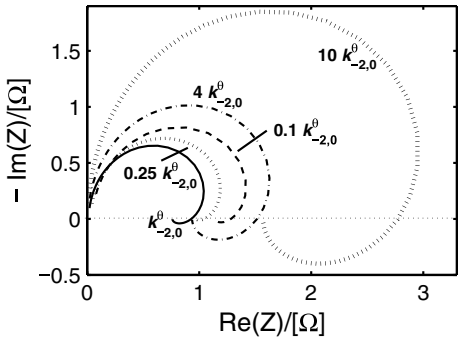

Fig. 10. EIS of the VCS Langmuir model with reaction rate constant $k_{-2,0}$ varied from the reference value $k^{\ominus}_{2,0}$.

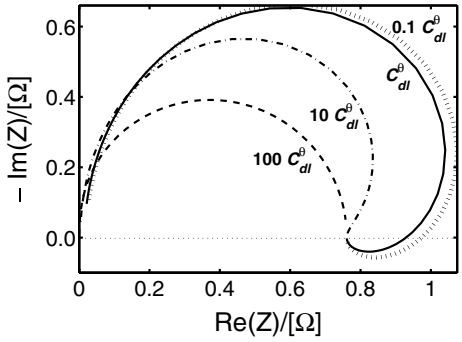

Fig. 11. EIS of the VCS Langmuir model with electrochemical double layer capacitance C_{dl} varied from the reference capacitance $C^{\ominus}_{dl}$.

Interpretation of a variation of the surface concentrations of Pt and Ru, c_{Pt} and c_{Ru}, is less transparent. Formally seen, the surface concentrations directly influence the reaction rate functions, hence also the steady-state behaviour. But since it is not possible, as mentioned above, to distinguish between the original reaction rate constants and the surface concentrations in steady-state measurements, the here used reaction rate constants are the product of original reaction rate constants and surface concentrations, e.g., $k_{1,0} \quad \text{const} \quad k_{1,orig} \cdot c_{Pt}$. Changing c_{Pt} or c_{Ru} implies therefore an externally not visible change in the internal composition of the reaction rate constants, which neither has an influence on the EIS nor on the steady-state. But, the given model formulation enables the definition of pure dynamic variables to study their influence on the EIS.

The variation of c_{Pt} is shown in Fig. 12. An increase in Pt surface concentration leads to a much larger pseudo-inductive behaviour. This increase in c_{Pt} lowers the time constant of the CO_{ads} balance equation, Eq. (5), which directly increases the dominant influence of reaction 1 and reaction 3 over reaction 2. The opposite holds for a decrease in c_{Pt}, where reaction 2 will dominate more strongly, and the pseudo-inductive behaviour disappears. Fig. 13, where a variation in Ru surface concentration is displayed, supports this. Increasing c_{Ru} has the same effect as decreasing c_{Pt}, namely a diminished pseudo-inductive behaviour, while a decrease in c_{Ru} gives a larger pseudo-inductive behaviour.

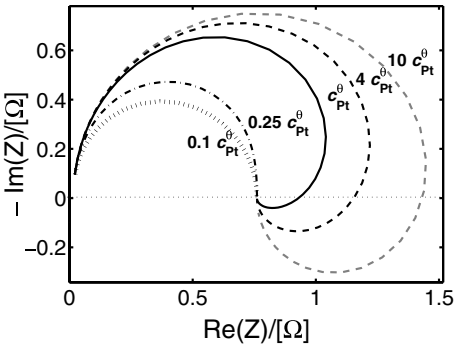

Fig. 12. EIS of the VCS Langmuir model with platinum surface concentration c_{Pt} varied from the reference platinum surface concentration $c_{\mathrm{Pt}}^{\ominus}$.

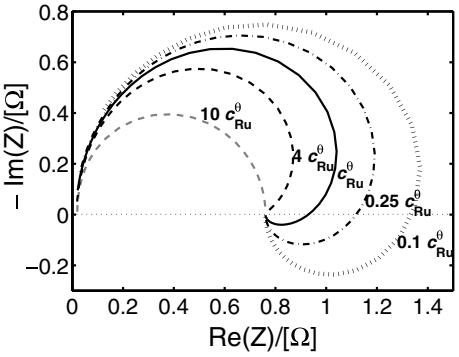

Fig. 13. EIS of the VCS Langmuir model with ruthenium surface concentration c_{Ru} varied from the reference ruthenium surface concentration $c_{\mathrm{Ru}}^{\ominus}$.

Since all storage constants influence the impedance spectra, and since the exact parameter values are not known, all of them should be included into the quantitative fitting procedure.

4.3.4. Variation of the inhomogeneity / interaction factors

Two of the four kinetic models contain Frumkin/Temkin descriptions. Hence, the influence of this adsorption/desorption type in contrast to the Langmuir adsorption/desorption is investigated in the following. Fig. 14 shows the influence of the inhomogeneity/interaction factors g_{CO} and g_{OH} on the impedance spectra. It can be observed that an increase in g_{CO} extinguishes the pseudo-inductive behaviour, while an increase in g_{OH} only increases the overall impedance. The variation of g_{CO} has a direct impact on the first and the third reaction step due to the exponential dependence of $k_1^{\mathrm{eff}}(\theta_{\mathrm{CO}})$ and $k_3^{\mathrm{eff}}(E,\theta_{\mathrm{CO}})$ on g_{CO}: in case of an increase in $k_1^{\mathrm{eff}}(\theta_{\mathrm{CO}})$, $k_3^{\mathrm{eff}}(E,\theta_{\mathrm{CO}})$ is decreased, and vice versa. Hence, the inhomogeneity factor g_{CO} causes a dominance of either step 1 or 3, which extinguishes the pseudo-inductive behaviour, as shown in Fig. 14. In the case of g_{OH}, the influence is less pronounced, since the factor will influence the EIS via the surface coverage of OH, as in the case of $k_{2,0}$ and $k_{2,0}$.

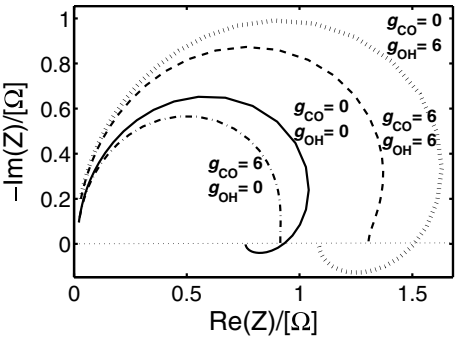

Fig. 14. EIS of the VCS Frumkin/Temkin model with inhomogeneity/interaction factors g_{CO} and g_{OH} varied from the reference inhomogeneity/interaction factors of the VCS Langmuir model ($g_{\mathrm{CO}} = 0, g_{\mathrm{OH}} = 0$).

4.3.5. Variation of potential

A change in potential strongly influences the effective reaction rate functions $k_i^{\mathrm{eff}}(E,\theta_{\mathrm{CO}},\theta_{\mathrm{OH}})$ for the reactions $i \in \{2,-2,3\}$, and it therefore shifts the relative dominance of the single steps. This is shown in Fig. 15, where the simulated impedance spectra for 0.44 and 0.37 V are displayed in comparison to the reference impedance spectrum at 0.41 V. The changes are qualitative and quantitative: With increasing anode potential, the impedance spectra become smaller due to the higher effective reaction rate functions $k_2^{\mathrm{eff}}(E)$ and $k_3^{\mathrm{eff}}(E)$. Besides changes in the overall size of the spectrum, the change in potential also shows an expected strong influence on the pseudo-inductive behaviour. An increase of potential to 0.44 V leads to a loss in pseudo-inductive behaviour. This can be explained by the different dependence of the effective reaction rate functions $k_i^{\mathrm{eff}}(E,\theta_{\mathrm{CO}},\theta_{\mathrm{OH}})$ on potential: While reaction 1 is potential independent, reaction 2 and reaction 3 depend on potential. This leads to a decrease in the relative dominance of the latter steps in the EIS for increasing potentials.

Qualitatively similar findings were observed for the VCS Frumkin/Temkin, Kauranen Langmuir and Kauranen Frumkin/Temkin kinetics.

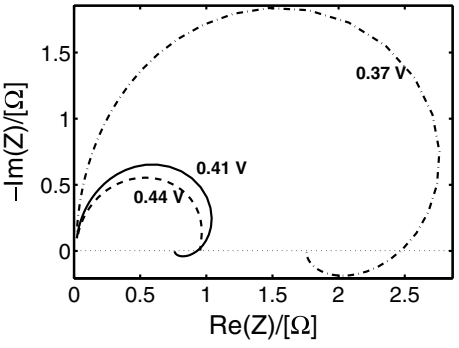

Fig. 15. EIS of the VCS Langmuir model with electrochemical potential E varied from the reference potential (0.41 V).

4.4. Quantitative model discrimination

The previous section showed the sensitivity of the modelled impedance spectra to the reaction rate constants $k_{i,0}$ ($i \in \{1,2,-2,3\}$), to the storage parameters C_{dl}, c_{Pt} and c_{Ru}, to the quasi-steady state potential E and, in case of Frumkin/Temkin adsorption, to the inhomogeneity/interaction factors g_{CO} and g_{OH}. In this section, each of the four models is best fitted to the experimental impedance data and to the steady-state currents. A comparison of the best results is used for quantitative model discrimination.

Since the EIS depends on the above mentioned parameters, all of them are optimised simultaneously. To include the potential dependence, a combined optimisation of the parameters to all three experimental EIS (i.e. at 0.37, 0.41 and 0.44 V) is conducted. As already shown (Figs. 7 15), the parameters are not linearily influencing the impedance spectra, and a variation in one parameter may annihilate the influence of the variation of others on the EIS. Since a local optimiser most probably finds only local minima, which in our case gave results with low accordance to the experiments, a global optimiser with an evolutionary strategy was used. In the objective function, higher single weights were given to experimental points in the pseudo-inductive region, to emphasise the importance of this region of the EIS for the methanol oxidation kinetics. For a similar reason, medium to low frequency points ($f < 2$ Hz) were only used for optimisation: at high frequencies, the electrode structure influence and the membrane influence dominate the EIS shape.

Fig. 4 shows the EIS optimisation result of the VCS Langmuir model (lines) in comparison to the experimental EIS (concatenated symbols). The respective parameter values are given in Table 1. All simulated curves show pseudo-inductive behaviour, but in contrast to the experimental EIS, this behaviour is not increasing with decreasing anode potential. Furthermore, the potential dependence of the size of the simulated impedance spectra is smaller than in experiments. This is especially distinctive with the simulated EIS at 0.44 and 0.41 V. The model results are close and even intersect at low frequencies. Taking all above mentioned points into consideration, a quantitative representation of the experimental EIS with the VCS Langmuir model seems not possible.

The optimisation result of the VCS-model with Frumkin/Temkin adsorption is displayed in Fig. 16 (parameter values see Table 1). For this model hold similar findings and conclusions as for the VCS Langmuir model: all curves show pseudo-inductive behaviour, but the potential dependence both of the EIS size and of the pseudo-inductive behaviour diverge from the experiments'. None-the-less, the potential dependence of the size of the EIS has slightly improved. This effect should be attributed to the exponential dependence of the reaction rates on the surface coverages of CO_{ads} and OH_{ads}.

In contrast to the VCS kinetic models, both Kauranen kinetic models show a higher accordance of experiment and simulation with regard to potential dependence. Fig. 17 displays the optimisation result for the Kauranen Langmuir model (parameter values see Table 1). The EIS at 0.41 and 0.37 V represent the experimental EIS much better than both VCS-models. None-the-less, the EIS at 0.44 V shows no pseudo-inductance, which should be due to the occurrence of an r.d.s. Since the loss of pseudo-inductive behaviour at high anode potentials was not reported for methanol oxidation experiments in the literature, this model would not pose a good approximation of the real dynamic behaviour at high potential.

In contrast to the former model, the Kauranen Frumkin/Temkin kinetic model produces pseudo-inductive behaviour at all potentials. Like in the experiments, this behaviour increases with decreasing potential.

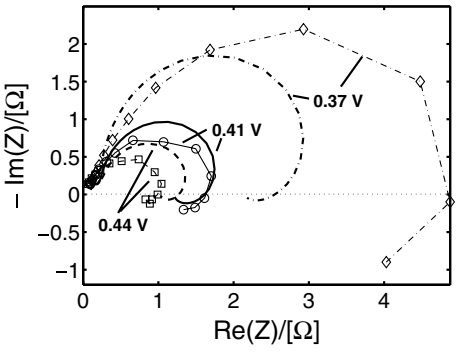

Fig. 16. Simulated EIS (lines) of the VCS Frumkin/Temkin model with optimised parameters (values see Table 1) vs. experimental EIS (concat enated symbols) at three potentials.

Table 1
Parameter results of the global optimisation for all four kinetic models

Parameter	VCS Langm.	VCS Frumk./T.	Kaur. Langm.	Kaur. Frumk./T.
$10^6\ k_{1,0}$/m s^{-1}	1.48	1.54	0.87	1.15
$10^5\ k_{2,0}$/mol m^{-2} s^{-1}	6.11	1.59	6.26	54.4
$k_{-2,0}$/mol m^{-2} s^{-1}	25.3	6.78	98,200	21,800
$10^6\ k_{3,0}$/mol m^{-2} s^{-1}	0.515	0.545	649,000	10,400
C_{dl}/F m^{-2}	8690	6350	18,100	9040
$10^2\ c_{Pt}$/mol m^{-2}	7.75	8.82	7.21	9.57
$10^2\ c_{Ru}$/mol m^{-2}	4.32	9.3	1.2	4.83
g_{CO}		0.293		3.72
g_{OH}		2.08		0.408

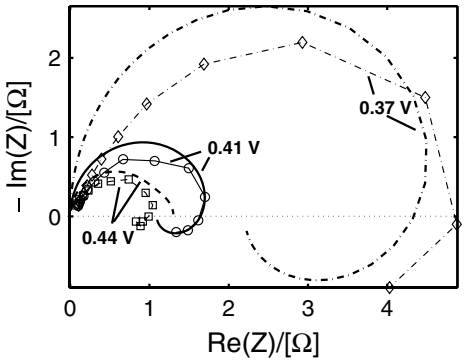

Fig. 17. Simulated EIS (lines) of the Kauranen Langmuir model with optimised parameters (values see Table 1) vs. experimental EIS (concat enated symbols) at three potentials.

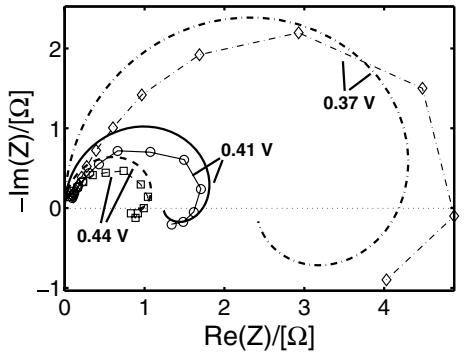

Fig. 18. Simulated EIS (lines) of the Kauranen Frumkin/Temkin model with optimised parameters (values see Table 1) vs. experimental EIS (concatenated symbols) at three potentials.

Furthermore, the model gives the best potential dependence of the EIS. The spectra are given in Fig. 18 (parameter values see Table 1).

Compared to the other kinetic descriptions, the Kauranen Frumkin/Temkin kinetics shows the best accordance of simulation with experiment. Hence, with respect to the four kinetic formulations, the Kauranen Frumkin/Temkin kinetics is identified as the kinetic model which can best describe the steady-state and the dynamic behaviour.

A comparison of all model parameters of Table 1 shows a relatively stable $k_{1,0}$, a similarly large $k_{3,0}$ for the VCS models, but a much larger $k_{3,0}$ for the Kauranen models. This results in similarly large $k_1^{\mathrm{eff}}(\theta_{\mathrm{CO}})$ and $k_3^{\mathrm{eff}}(E,\theta_{\mathrm{CO}})$ for the VCS models $(0.65 \leqslant k_1^{\mathrm{eff}}(E,\theta_{\mathrm{CO}})/k_3^{\mathrm{eff}}(E,\theta_{\mathrm{CO}}) \leqslant 4.28)$ in the contemplated potential region, but $k_1^{\mathrm{eff}}(\theta_{\mathrm{CO}})$ is much smaller than $k_3^{\mathrm{eff}}(\theta_{\mathrm{CO}})$ for the Kauranen models $(k_1^{\mathrm{eff}}(\theta_{\mathrm{CO}})/k_3^{\mathrm{eff}}(\theta_{\mathrm{CO}}) \leqslant 0.12)$. Although this suggests that the first reaction step is dominating in the Kauranen models, which would contradict the interpretation of the pseudo-inductive behaviour, this is not the case: The equilibrium of the second reaction step in the Kauranen models is strongly shifted to the left, causing a lower OH surface coverage ($\leqslant$0.15). As a result, reaction step 3 is decelerated.

5. Conclusions

The reproduction of dynamic methanol oxidation kinetic measurements by a kinetic description is essential for modelling of the dynamic behaviour of DMFCs. This paper presented such a dynamics analysis of the methanol oxidation kinetics on a DMFC anode. Four different kinetic descriptions for methanol oxidation were investigated. They differ in the adsorption/desorption mechanisms, as well as in the potential dependence of a reaction step. Since all kinetic descriptions quantitatively describe the experimental steady-state behaviour, dynamic measurements, here electrochemical impedance spectroscopy, is used to identify the most adequate model.

The EIS of the four kinetic descriptions were modelled by using their frequency domain transformed balance equations. Analysis of the dependence of the modelled impedance spectra on parameter variation showed that there is a narrow range at which pseudo-inductive behaviour is produced: at least two consecutive steps with similar dynamic reaction rates have to be involved. In the models presented in this paper, these steps were the methanol partial oxidation and the oxidation of the adsorbed intermediate, while a further reaction parallel to the methanol partial oxidation was in quasi equilibrium and influences the EIS only indirectly via the surface coverage θ_{OH}. Besides the reaction rate constants, the storage parameters and the potential dependence also showed a strong influence on the impedance spectra.

These findings were used during global parameter optimisation of all four kinetic descriptions. A comparison of the resulting EIS lead to the identification of the Kauranen Frumkin/Temkin kinetics as the best quantitative description of the steady-state and dynamic electrochemical methanol oxidation. In subsequent works, this kinetic description will be used for modelling the dynamic behaviour of whole DMFCs.

References

[1] A. Arico, S. Srinivasan, V. Antonucci, Fuel Cells 1 (2) (2001) 133 161.
[2] V. Bagotzky, Y. Vassiliev, O.A. Khazova, J. Electroanal. Chem. 81 (1977) 229 238.
[3] X. Xia, T. Iwasita, F. Ge, W. Vielstich, Electrochim. Acta 41 (5) (1996) 711 718.
[4] J. Leger, J. Appl. Electrochem. 31 (2001) 767 771.
[5] T. Housmans, M. Koper, J. Phys. Chem. B 107 (2003) 8557 8567.
[6] T. Vidakovic', M. Christov, K. Sundmacher, J. Electroanal. Chem. 580 (2005) 105 121.
[7] P. Kauranen, E. Skou, J. Munk, J. Electroanal. Chem. 404 (1996) 1 13.
[8] H. Gasteiger, N. Markovic', P. Ross, E. Cairns, J. Electrochem. Soc. 141 (7) (1994) 1795 1803.
[9] H. Hoster, T. Iwasita, H. Baumgartner, W. Vielstich, J. Electrochem. Soc. 148 (2001) A496 A501.
[10] Z. Jusys, J. Kaiser, R. Behm, Electrochim. Acta 47 (2002) 3693 3706.
[11] D. Kardash, C. Korzeniewski, N. Markovic', J. Electroanal. Chem. 500 (2001) 518 523.

[12] A. Kabbabi, R. Faure, R. Durand, B. Beden, F. Hahn, J. Leger, C. Lamy, J. Electroanal. Chem. 444 (1998) 41 53.
[13] H. Wang, C. Wingender, H. Baltruschat, M. Lopez, M.T. Reetz, J. Electroanal. Chem. 509 (2001) 163 169.
[14] A. Lima, C. Coutanceau, J. Leger, C. Lamy, J. Appl. Electrochem. 31 (2001) 379 386.
[15] M. Gotz, H. Wendt, Electrochim. Acta 43 (24) (1998) 3637 3644.
[16] B. Gurau, R. Viswanathan, R. Liu, T. Lafrenz, K. Ley, E.S. Smotkin, J. Phys. Chem. B 102 (1998) 9997 10003.
[17] M. Watanabe, S. Motoo, J. Electroanal. Chem. 60 (1975) 267 273.
[18] T. Jarvi, E. Stuve, Fundamental aspects of vacuum and electrocat alytic reactions of methanol and formic acid on platinum surfaces, in: J. Lipkowski, P. Ross (Eds.), Electrocatalysis, Wiley VCH, New York, 1998 (Chapter 3).
[19] A. Hamnett, Mechanism of methanol electrooxidation, in: A. Wieckowski (Ed.), Interfacial Electrochemistry, Theory, Experi ment, and Applications, Marcel Decker Inc., New York, 1999 (Chapter 47).
[20] U. Krewer, K. Sundmacher, Transfer function analysis of the dynamic behaviour of DMFCs: response to step changes in cell current, J. Power Sources 154 (1) (2006) 153 170.
[21] V. Gogel, T. Frey, Z. Yongsheng, K. Friedrich, L. Joerissen, J. Garche, J. Power Sources 127 (2004) 172 180.
[22] J. Divisek, J. Fuhrmann, K. Gartner, R. Jung, J. Electrochem. Soc. 150 (6) (2003) A811 A825.
[23] J. Meyers, J. Newman, J. Electrochem. Soc. 149 (6) (2002) A718 A728.
[24] P. Argyropoulos, K. Scott, J. Power Sources 137 (2) (2004) 228 238.
[25] S. Zhou, T. Schultz, M. Peglow, K. Sundmacher, Phys. Chem. Chem. Phys. 3 (2001) 347 355.
[26] K. Sundmacher, T. Schultz, S. Zhou, K. Scott, M. Ginkel, E. Gilles, Chem. Eng. Sci. 56 (2001) 333 341.
[27] J. Nordlund, G. Lindbergh, J. Electrochem. Soc. 149 (9) (2002) A1107 A1113.
[28] W. Lin, M. Zei, M. Eiswirth, G. Ertl, T. Iwasita, W. Vielstich, J. Phys. Chem. B 103 (1999) 6968 6977.
[29] K. Friedrich, K. Geyzers, U. Linke, U. Stimming, J. Stumper, J. Electroanal. Chem. 402 (1996) 123 128.
[30] V. Panic', T. Vidakovic', S. Gojkovic', A. Dekanski, S. Milonjic', B. Nikolic', Electrochim. Acta 48 (2003) 3805 3813.
[31] A. Mitterdorfer, L. Gauckler, Solid State Ionics 117 (3 4) (1999) 187 202.
[32] B. Bequette, Process Dynamics: Process Modelling, Analysis, and Simulation, Prentice Hall PTR, New Jersey, 1998.
[33] A. Mutambara, Design and Analysis of Control Systems, CRC Press, Boca Raton, 1999.
[34] E. Gileadi, Kinetics for Chemists, Chemical Engineers and Material Scientists, Wiley VCH, New York, 1993.
[35] H. Dinh, X. Ren, F. Garzon, P. Zelenay, S. Gottesfeld, J. Electroanal. Chem. 491 (2000) 222 233.